Mon. Not. R. Astron. Soc. **000**, 1–12 (2016) Printed 21 October 2016 (MN LATEX style file v2.2)

NIHAO XII: galactic uniformity in a ΛCDM universe

Aaron A. Dutton,[1⋆] Aura Obreja[1], Liang Wang[2,3], Thales A. Gutcke[4], Tobias Buck[4], Silviu M. Udrescu[1], Jonas Frings[4], Gregory S. Stinson[4], Xi Kang[2], Andrea V. Macciò[1,4]

[1] *New York University Abu Dhabi, PO Box 129188, Abu Dhabi, United Arab Emirates*
[2] *Purple Mountain Observatory, 2 West Beijing Road, Nanjing 210008, China*
[3] *International Centre for Radio Astronomy Research (ICRAR), M468, University of Western Australia, 35 Stirling Hwy, Crawley, WA 6009, Australia*
[4] *Max-Planck-Institut für Astronomie, Königstuhl 17, 69117 Heidelberg, Germany*

arXiv:1610.06375v1 [astro-ph.GA] 20 Oct 2016

submitted to MNRAS

ABSTRACT

We use a sample of 83 high-resolution cosmological zoom-in simulations and a semi-analytic model to study the stocasticity of galaxy formation in haloes ranging from dwarf ($M_{200} \sim 10^{10}$M$_\odot$) to Milky Way ($M_{200} \sim 10^{12}$M$_\odot$) masses. Our simulated galaxies reproduce the observed inefficiency of galaxy formation as expressed through the stellar, gas and baryonic Tully-Fisher (TF) relations. The scatter in our simulated TF relations is very small, and velocity dependent. For HI velocities in the range ($70 \lesssim V \lesssim 220$ km/s), the scatter is just 0.08 to 0.14 dex, consistent with the observed intrinsic scatter. At low velocities ($20 \lesssim V \lesssim 70$ km/s), the simulated scatter is 0.2-0.25 dex, which could be tested with future observations. The scatter in the stellar mass vs dark halo velocity relation is constant for $30 \lesssim V \lesssim 200\,\mathrm{km\,s^{-1}}$, and smaller ($\simeq 0.17$ dex) when using the maximum circular velocity of the dark matter only simulation, $V_{\rm max}^{\rm DMO}$, compared to the virial velocity (V_{200} or $V_{200}^{\rm DMO}$). The scatter in stellar mass is correlated with halo concentration, and is minimized when using a circular velocity at a fixed fraction of the virial radius $\simeq 0.4R_{200}$ or with $V_\alpha = V_{200}^{\rm DMO}(V_{\rm max}^{\rm DMO}/V_{200}^{\rm DMO})^\alpha$ with $\alpha \simeq 0.7$, consistent with constraints from halo clustering. This uniformity in galaxy formation efficiency we see in our hydrodynamical simulations and a semi-analytic model proves the simplicity and self-regulating nature of galaxy formation in a ΛCDM universe.

Key words: dark matter – galaxies: fundamental parameters – galaxies: haloes – galaxies: kinematics and dynamics – methods: numerical

1 INTRODUCTION

Galaxies come in a wide variety of sizes, shapes, and masses, yet their structural properties obey a number of scaling relations – hinting at an underlying simplicity to the seemingly haphazard process of galaxy formation in a hierarchical universe. The correlation between dynamics and luminosity is fundamental, due to its small scatter, and the link it provides between baryons and dark matter. This relation is known as the Tully-Fisher (TF, Tully & Fisher 1977) and Faber-Jackson (FJ, Faber & Jackson 1976) relation, for spiral/late-type/star forming and elliptical/early-type/quiescent galaxies, respectively. In the original studies the dynamics was traced by the linewidth of the 21cm line of neutral hydrogen (HI) for spiral galaxies, and by the stellar velocity dispersion for elliptical galaxies. In more recent studies, luminosity has been replaced by stellar or baryonic (defined as stars plus neutral gas) mass (e.g., McGaugh et al. 2000; Bell & de Jong 2001), with these relations often being referred to as the stellar and baryonic Tully-Fisher relations, respectively. In order to put all types of galaxies onto the same relation circular velocities measured at the same fiducial radius can be used (Dutton et al. 2010, 2011).

The TF relation is a benchmark for any successful theory of galaxy formation. The slope naturally arises in Cold Dark Matter (CDM) based galaxy formation models (e.g., Mo et al. 1998; Navarro & Steinmetz 2000; Dutton et al. 2007), but reproducing the normalization has been more challenging, with models invariably predict-

⋆ dutton@nyu.edu

© 2016 RAS

ing higher rotation velocities at fixed stellar mass than observed (e.g. Navarro & Steinmetz 2000; Governato et al. 2007; Marinacci et al. 2014). A contributor to this problem is when simulated galaxies are too compact. However, Dutton et al. (2007, 2011) showed that when models are constrained to reproduce the sizes of galaxies, they also overpredict the circular velocities if haloes contract in response to galaxy formation (Blumenthal et al. 1986; Gnedin et al. 2004). Such a conclusion has been verified by subsequent studies (e.g., Desmond & Wechsler 2015; Chan et al. 2015).

A close relative of the Tully-Fisher relation is that between galaxy stellar mass and dark halo mass. The $M_{\rm star}$ vs $M_{\rm halo}$ relation has been studied extensively using observations of weak gravitational lensing, satellite kinematics, and halo abundance matching (e.g., Yang et al. 2003; Mandelbaum et al. 2006; Conroy & Wechsler 2009; Moster et al. 2010; More et al. 2011; Leauthaud et al. 2012; Behroozi et al. 2013; Hudson et al. 2015). One of the key results of these studies is that star formation is inefficient. The maximum efficiency is $\approx 25\%$, and independent of redshift, occurring at a halo mass similar to that of the Milky Way (i.e., $\sim 10^{12}{\rm M}_\odot$). At both higher and lower halo masses the efficiency drops even further.

The scatter in stellar mass at fixed halo mass is hard to quantify observationally (since halo masses cannot be reliably measured for individual galaxies), but it is estimated to be small, $\approx$ 0.20 dex, and independent of halo mass (More et al. 2011; Reddick et al. 2013). Note that the scatter in halo mass at fixed stellar mass is not a constant, rather it increases with stellar mass due to the shallowing slope of the $M_{\rm star} - M_{\rm halo}$ relation at high halo masses. Likewise, the observed scatter in the TF relation is small $\approx$ 0.20 dex in mass (or luminosity) at fixed velocity (Courteau et al. 2007; Reyes et al. 2011; McGaugh 2012). The maximum scatter in the stellar-to-halo mass ratio allowed by the TF relation is slightly larger than the observed scatter, since variation in stellar-to-halo mass partially moves galaxies along the TF relation (Dutton et al. 2007). However, contributions from variation in dark halo concentrations, stellar mass-to-light ratios (both intrinsic variations and measurement uncertainties) reduce the allowed scatter to less than 0.2 dex.

The best tracer of halo masses for individual galaxies comes from galaxy rotation velocities at large galactic radii from the 21 cm line of neutral hydrogen. The Baryonic Tully-Fisher relation (BTF) is a correlation between the baryonic mass of a galaxy, $M_{\rm bar}$, (stars plus cold gas) and the rotation velocity at large radii, $V_{\rm flat}$, (typically in the flat part of the rotation curve). It is an extension of the original linewidth - luminosity relation of Tully & Fisher (1977). Since the observed rotation velocity is related to the halo virial velocity (Dutton et al. 2010), the BTF provides the most direct observational constraint on the efficiency of galaxy formation. The observed scatter in the BTF is $\simeq$ 0.22 dex in baryonic mass at fixed rotation velocity (McGaugh 2012; Lelli et al. 2016). Accounting for measurement uncertainties the intrinsic scatter is $\simeq$ 0.10 dex. Using a semi-analytic model (Dutton & van den Bosch 2009) for disk galaxy formation, Dutton (2012) found a model scatter of $\simeq$ 0.15 dex. Since this model makes some simplifying assumptions (such as smooth mass accretion histories), one might expect it to underestimate the true scatter. Thus, there is a potential conflict between the observed and predicted scatter in the BTF.

Galaxy formation is observed to be both inefficient, yet remarkably uniform. Is it possible to reproduce this in a ΛCDM structure formation scenario? Which definition of galaxy mass and halo mass are most tightly correlated? To address these questions we study the relations between galaxy mass and circular velocity in a new sample of high-resolution cosmological simulations ($\sim 10^6$ particles per galaxy) from the NIHAO (Numerical Investigation of a Hundred Astrophysical Objects) project (Wang et al. 2015). This paper is organized as follows: The NIHAO simulations and derived galaxy properties are described in §2, the velocity mass relations are shown in §3, implications for halo abundance matching are shown in §4, and the conclusions in §5.

2 GALAXY FORMATION SIMULATIONS

Here we briefly describe the NIHAO simulations. We refer the reader to Wang et al. (2015) for a complete discussion. NIHAO is a sample of $\sim$ 90 hydrodynamical cosmological zoom-in simulations using the SPH code GASOLINE (Wadsley et al. 2004) with improvements to the hydrodynamics as described in Keller et al. (2014). Haloes are selected from parent dissipationless simulations of size 60, 20, & 15 Mpc/h, presented in Dutton & Macciò (2014) which adopt a flat ΛCDM cosmology with parameters from the Planck Collaboration et al. (2014): Hubble parameter H_0= 67.1 $\rm km\,s^{-1}\ Mpc^{-1}$, matter density $\Omega_{\rm m} = 0.3175$, dark energy density $\Omega_\Lambda = 1 - \Omega_{\rm m} = 0.6825$, baryon density $\Omega_{\rm b} = 0.0490$, power spectrum normalization $\sigma_8 = 0.8344$, power spectrum slope $n = 0.9624$. Haloes are selected uniformly in log halo mass from ~ 10 to ~ 12 *without* reference to the halo merger history, concentration or spin parameter. Star formation and feedback is implemented as described in Stinson et al. (2006, 2013). Mass and force softening are chosen to resolve the mass profile at $\lesssim 1\%$ the virial radius, which results in $\sim 10^6$ dark matter particles inside the virial radius of all haloes at $z = 0$. The motivation of this choice is to ensure that the simulations resolve the galaxy dynamics on the scale of the half-light radii, which are typically $\sim 1.5\%$ of the virial radius (Kravtsov 2013).

Each hydro simulation has a corresponding dark matter only (DMO) simulation of the same resolution. In some cases these simulations are in different evolutionary states, due to a major merger occurring at a different time. In order for a fair comparison between hydro and DMO simulations, we remove four haloes for which there is a large difference between the halo masses in the hydro and DMO simulations. In addition we remove the three most massive haloes (g1.77e12, g1.92e12, g2.79e12), as there is evidence that these have formed too many stars, in particular near the galaxy centers. The final sample consists of 83 simulations.

2.1 Derived galaxy and halo parameters

Haloes in NIHAO zoom-in simulations were identified using the MPI+OpenMP hybrid halo finder `AHF`[1] (Gill et al. 2004;

[1] http://popia.ft.uam.es/AMIGA

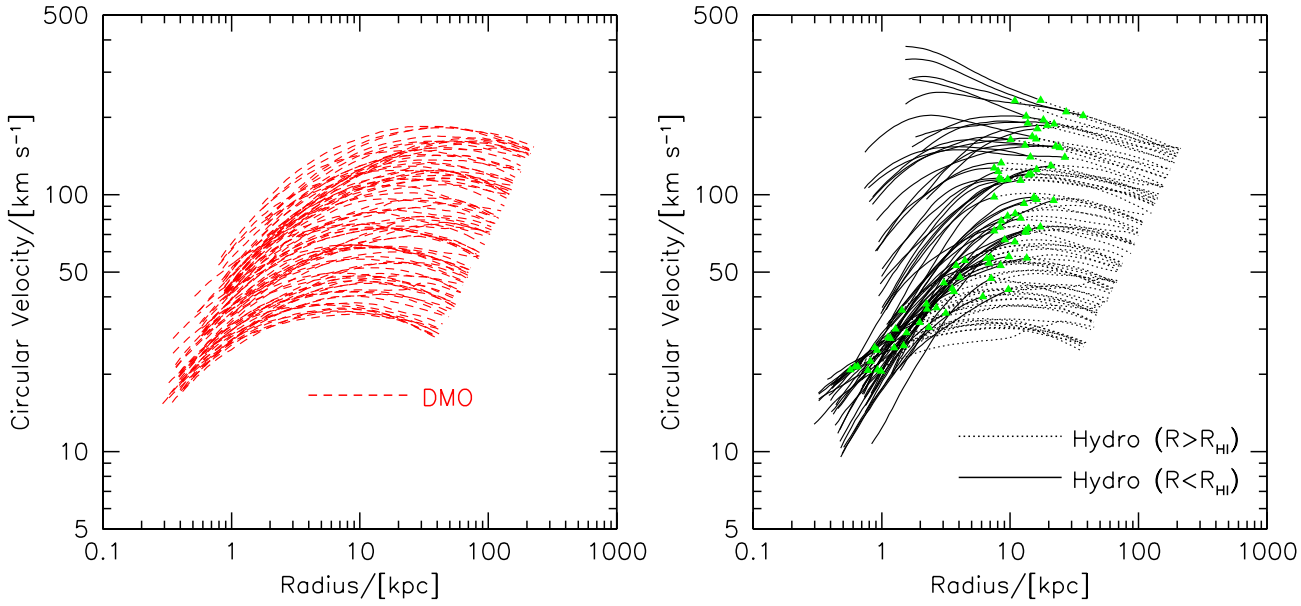

Figure 1. Circular velocity profiles for the primary simulated galaxies used in this paper. Lines are plotted out to the virial radius. Black lines show circular velocity for hydrodynamical simulations, solid lines for radii smaller than the HI radius, dashed for larger radii, red dashed lines show circular velocity for the dark matter only simulations. The circular velocity at the HI radius is shown with a green triangle. There is more variety in the profiles from the hydro simulations at radii below $\sim 0.1R_{200}$.

Knollmann & Knebe 2009). **AHF** locates local over-densities in an adaptively smoothed density field as prospective halo centers. The virial masses of the haloes are defined as the masses within a sphere whose average density is 200 times the cosmic critical matter density, $\rho_{\rm crit} = 3H_0^2/8\pi G$. The virial mass, size and circular velocity of the hydro simulations are denoted: $M_{200}, R_{200}, V_{200}$. The corresponding properties for the dark matter only simulations are denoted with a superscript, DMO. For the baryons we calculate masses enclosed within spheres of radius $r_{\rm gal} = 0.2R_{200}$. The stellar mass inside $r_{\rm gal}$ is $M_{\rm star}$, the neutral gas inside $r_{\rm gal}$ is $M_{\rm neut} \equiv 1.33M_{\rm HI}$, where the neutral hydrogen, HI , mass is computed following Rahmati et al. (2013) as described in Gutcke et al. (2016). The galaxy baryonic mass is defined as $M_{\rm gal} = M_{\rm star} + M_{\rm neut}$, while the virial baryonic mass $M_{\rm bar}$ is all of the stars and gas within R_{200}.

We measure the circular velocity at a number of radii as discussed below.

2.2 Definitions of Circular Velocity

Since the circular velocity profiles of galaxies are not constant, the choice of circular velocity one adopts will impact the slope, zero point and scatter of the TF relation (e.g., Brook et al. 2016; Bradford et al. 2016). Depending on the goals of the study different definitions should be adopted. For example, measurements at small radii are more sensitive to the distribution of the baryons and the halo response, while measurements at large radii are a better probe of the halo mass.

Fig. 1 shows circular velocity profiles, $V_{\rm circ} = \sqrt{GM(r)/r}$, for the primary galaxy in each zoom-in simulation. It shows the diversity of circular velocity profiles of the hydro simulations (black solid lines), compared to the dissipationless simulations (red dashed lines). In particular, at small radii, both lower and higher velocities (relative to the dissipationless simulations) are seen. The lower velocities

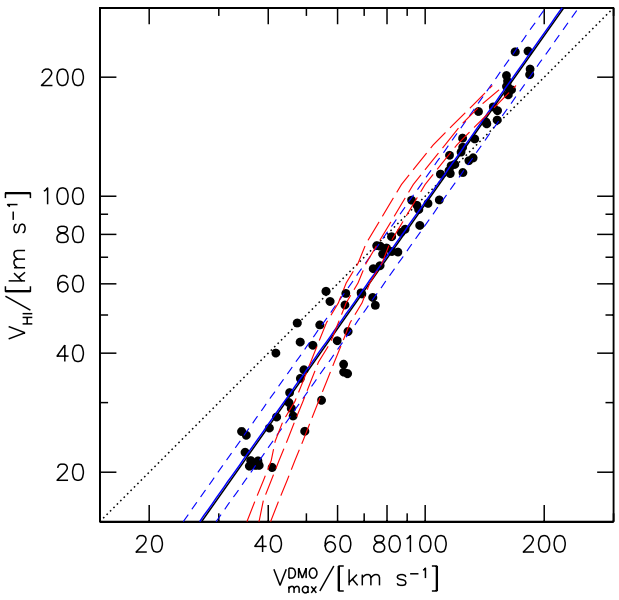

Figure 2. Relation between circular velocity at the HI radius, $V_{\rm HI}$, and the maximum circular velocity of the DMO simulation, $V_{\rm max}^{\rm DMO}$. Points show NIHAO simulations, dotted line shows the 1:1 relation, blue lines show a power-law fit with 1σ scatter, red lines show results from halo abundance matching (Papastergis et al. 2015).

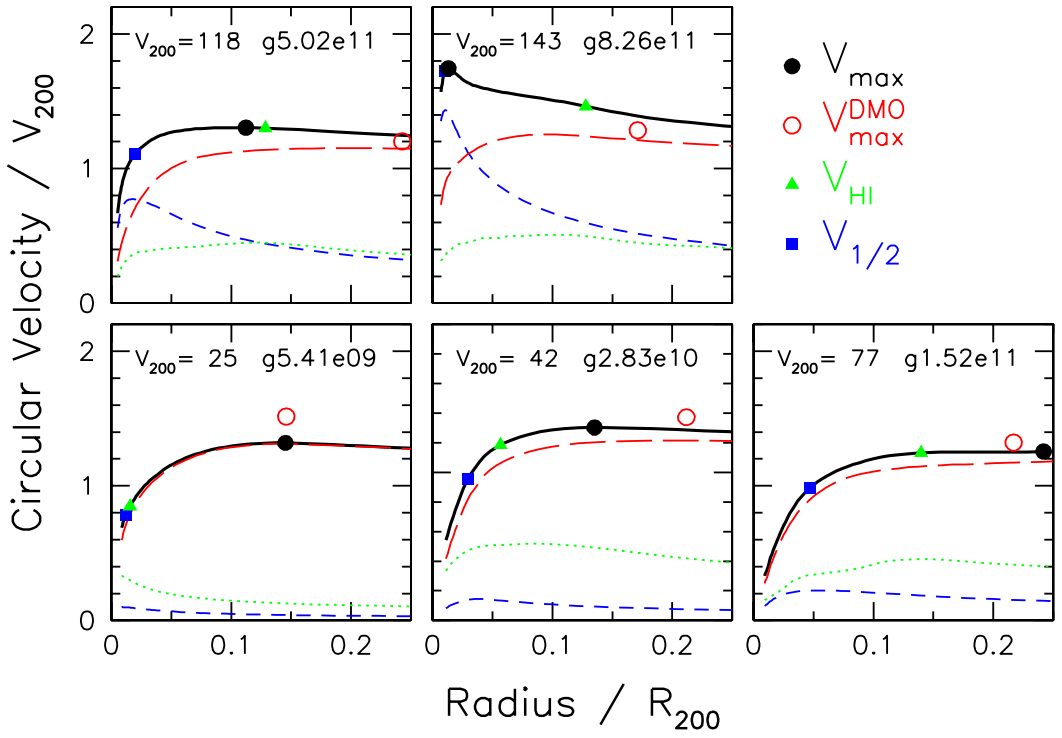

Figure 3. Example circular velocity profiles ordered by halo virial velocity, V_{200}. The various lines correspond to the total (black solid), dark matter (red long-dashed), stars (blue short dashed), gas (green dotted) components. Symbols show a variety of characteristic circular velocities $V_{1/2}$ (measured at the radius enclosing 50% of the stellar mass, blue square), $V_{\rm HI}$ (measured at the radius enclosing 90% of the HI gas, green triangle), $V_{\rm max}$ (maximum circular velocity of the hydro simulation, black circle), and $V_{\rm max}^{\rm DMO}$ (maximum circular velocity of the DMO simulation, red open circle). The HI radius typically occurs in the flat part of the rotation curve, except for the lowest mass galaxies.

are due to expansion of the dark matter halo (Dutton et al. 2016; Tollet et al. 2016), while the higher velocities are primarily due to collapse of baryons. The green triangles show the circular velocity at the HI radius, $R_{\rm HI}$, which is defined to enclose 90% of the HI flux in a face-on projection. This typically occurs at $\sim 10\%$ of the virial radius, except for the lowest mass galaxies where the HI radius occurs at a smaller fraction of the virial radius due to a significant amount of the cold gas $T \lesssim 30000$K being ionized.

The HI velocity typically traces the maximum circular velocity of the dark matter only simulation (Fig. 2), again with the exception of the low mass galaxies. The relation between $V_{\rm HI}$ and $V_{\rm max}^{\rm DMO}$ is well fitted with a power-law with a slope steeper than unity:

$$\log_{10}\left(\frac{V_{\rm HI}}{[\,{\rm km\,s^{-1}}]}\right) = 1.83{+}1.42\left[\log_{10}\left(\frac{V_{\rm max}^{\rm DMO}}{[\,{\rm km\,s^{-1}}]}\right) - 1.89\right] \quad (1)$$

with a scatter of 0.06 dex in $V_{\rm HI}$ at fixed $V_{\rm max}^{\rm DMO}$. For comparison, the red lines show the relation between $V_{\rm HI}$ and $V_{\rm max}^{\rm DMO}$ applying halo abundance matching to the velocity function (Papastergis et al. 2015), which encouragingly broadly agrees with the NIHAO simulations. There are some caveats in a direct comparison, see Macciò et al. (2016) for a more detailed discussion. Briefly, the observed velocity function is based on HI linewidths, which does not necessarily trace the circular velocity at the HI radius. An inclination correction is applied in Papastergis et al. (2015) assuming thin rotating disks, whereas, there can be non-negligible pressure support especially in low mass galaxies. The abundance matching assumes no scatter in galaxy velocity at fixed halo velocity, whereas simulations find a large scatter.

Fig. 3 shows a representative sample of 5 circular velocity curves for haloes with virial velocity ranging from $V_{200} = 25\,{\rm km\,s^{-1}}$ to $V_{200} = 143\,{\rm km\,s^{-1}}$. The thick black lines show the total circular velocity, which is broken down into the contributions from stars (blue short-dashed lines), dark matter (red long-dashed lines), and gas (green dotted lines). Low mass haloes are dark matter dominated at all radii. The baryons and in particular the stars make a larger contribution in more massive haloes. In haloes with $V_{200} \gtrsim 100\,{\rm km\,s^{-1}}$ the baryons dominate the center.

For each galaxy circular velocities at four radii are shown: $V_{1/2}$ (blue square) measured at the radius enclosing (within a sphere) half the stellar mass; $V_{\rm HI}$ (green filled triangle) measured at the HI radius; $V_{\rm max}$ (black circle) the maximum circular velocity of the hydro simulation, and $V_{\rm max}^{\rm DMO}$ (red open circle) the maximum circular velocity of the dark matter only simulation. The stars are confined to a few percent of the virial radius, and thus the $V_{1/2}$ typically traces the rising part of the velocity profile. The HI radius typically occurs at 5-15 percent of the virial radius, and thus traces the "flat" part of the rotation curve. $V_{\rm HI}$ is typically

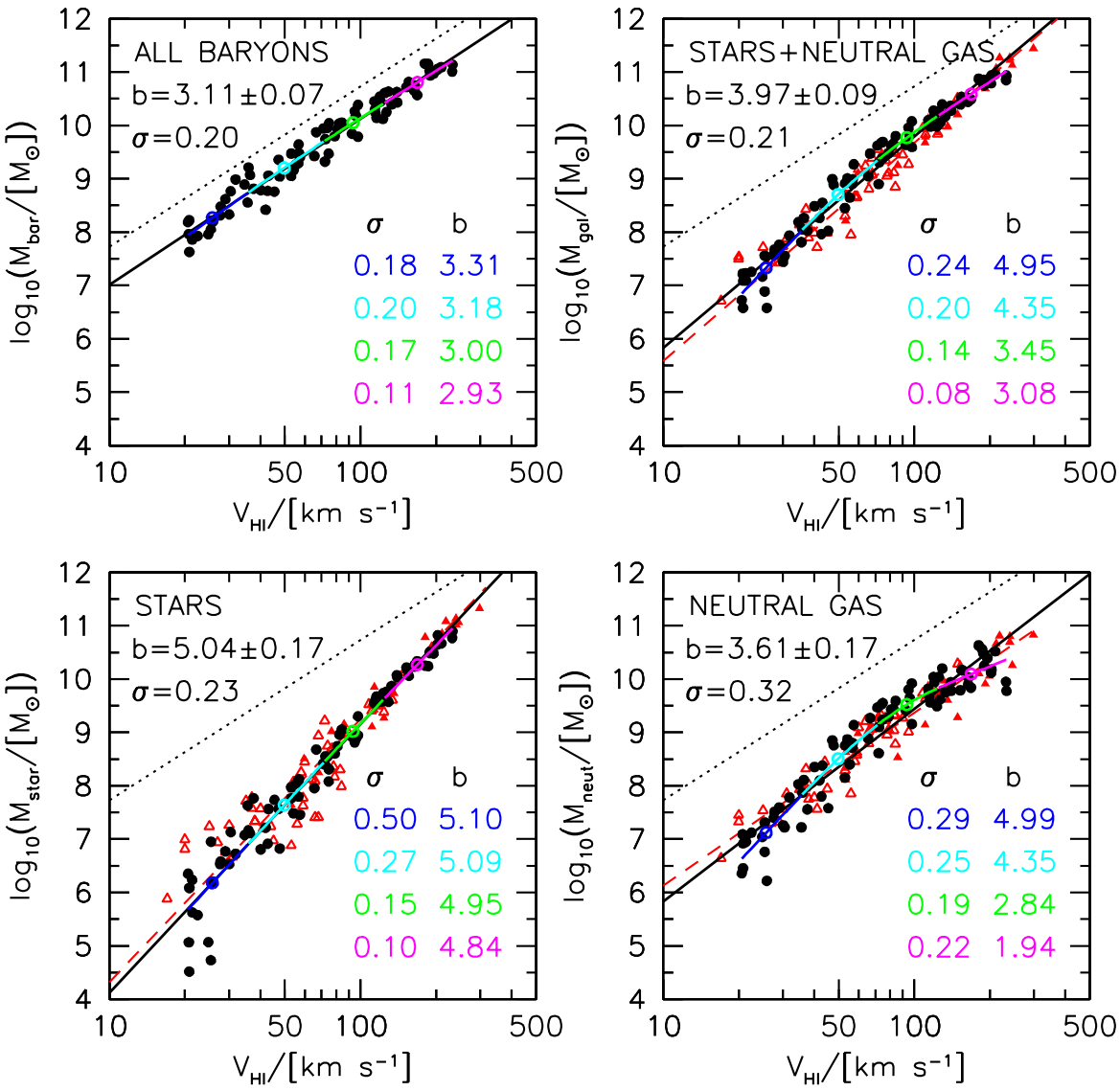

Figure 4. Tully-Fisher (TF) relations for velocities measured at the HI radius (in NIHAO simulations, black filled circles), and in the "flat" part of the rotation curve for observations (red triangles). Upper left: total baryonic mass within the virial radius, $M_{\rm bar}$; Upper right: stellar+neutral gas, $M_{\rm gal}$; Lower left: stellar mass, $M_{\rm star}$; Lower right: neutral gas, $M_{\rm gas}$. Observations are shown from McGaugh (2012, open triangles) & McGaugh & Schombert (2015, filled triangles). For reference, the dotted line shows the virial relation for reference: $M_{\rm b} = \Omega_{\rm b}/\Omega_{\rm m} V^3/hG$. The numbers in the upper left corner of each panel give the slope, b, and scatter, σ, for a global straight line fit (shown with solid black line). The lower right corner gives the slope and scatter for fits in quartiles of velocity (shown as colored lines).

20 to 40 percent higher than the virial velocity, V_{200}. The maximum circular velocity of the DMO simulation occurs at ~ 20 percent of the virial radius, and thus can often be approximated by $V_{\rm HI}$.

3 TULLY FISHER RELATIONS

We now construct various Tully Fisher relations. We fit these relations with a straight line $y = a + b(x - x_0)$ using linear least squares. Here x_0 is the mean of x. In general the independent variable is the logarithm of a velocity $x = \log_{10}(V/[\,{\rm km\,s^{-1}}])$, while the dependent variable is the logarithm of a mass $y = \log_{10}(M/[{\rm M}_\odot])$. We estimate uncertainties on a and b using jackknife re-sampling. We calculate the scatter about the best fit relation using the 68th percentile of the absolute residuals, p_{68}, which is less sensitive than the standard deviation to outlier points.

To gauge the dependence of the slopes and scatter on velocity we divide the velocities into quartiles and fit each quartile independently. This yields a mean value of y in four velocity bins which we spline interpolate to create a mean relation across the full x range. This ensures continuity in

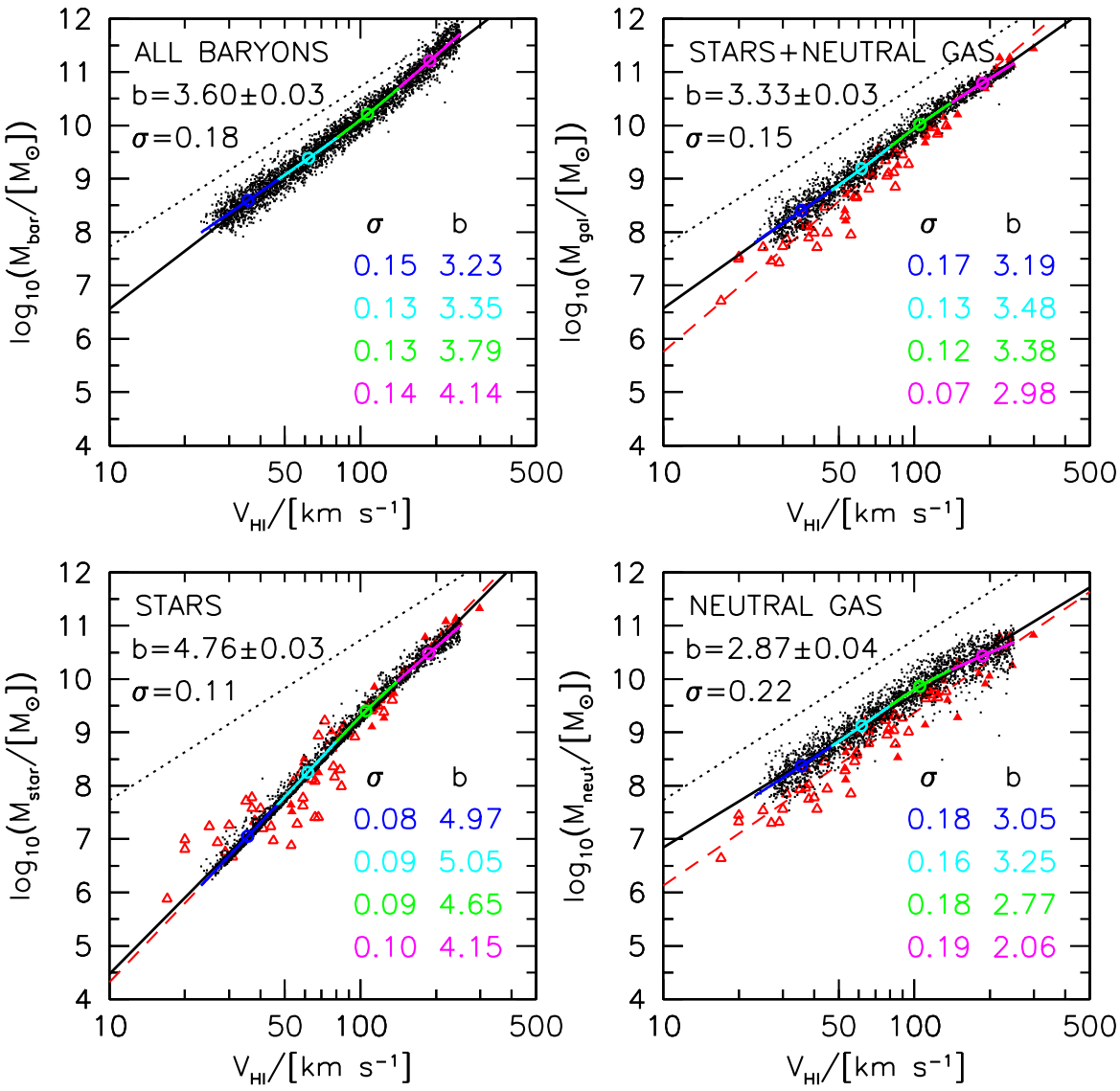

Figure 5. As Fig. 4 but using the semi-analytic model (black dots) of Dutton (2012).

the mean relations across the bin boundaries. We then calculate the scatter about this mean relation, and the local slopes in the four velocity bins. The slopes and scatter in each velocity quartile are shown in the lower right corner of Fig. 4.

3.1 Comparison with observed TF relations

We start with a comparison with observations, and thus use the observationally accessible $V_{\rm HI}$. In Fig. 4 black filled circles are the NIHAO simulations, while red open and solid triangles show observations from McGaugh (2012) and McGaugh & Schombert (2015), respectively. For the data from McGaugh & Schombert (2015) stellar masses are obtained from $3.6\mu m$ photometry assuming a stellar mass-to-light ratio of 0.45. For the observations $V_{\rm HI}$ is measured in the "flat" part of the HI rotation curve. Recall, that in the simulations it is measured at a radius enclosing 90% of the neutral gas. A potentially important caveat to our comparison is the observations are using rotation velocities, while in the simulations we are using (spherically symmetric) circular velocity.

As we will see, in general there is good agreement between the simulations and observations, although in detail there are differences. We discuss each of the Tully-Fisher relations in turn below. In summary the simulations have plausible amounts of stars and cold gas over a wide range of halo masses, and thus can be used to inform us about the stocasticity of galaxy formation in a ΛCDM universe.

As an additional reference point for the expectations for these scaling relations in a ΛCDM universe we show the results from the semi-analytic model (SAM) of Dutton (2012), updated here using the Planck cosmology, in Fig. 5. The SAM and NIHAO simulations give similar results. For

example, the stellar TF relation is steepest, while gas TF relation is the shallowest.

Stellar TF relation: There is a good agreement between observations and NIHAO simulations of the stellar TF relation (lower left panel). Simulations have a slope of 5.04±0.17, while observations have 4.93±0.17. The total scatter in the simulations is 0.23 dex, and the intrinsic scatter in the observations is 0.15 dex (McGaugh & Schombert 2015). However, the scatter is clearly mass dependent both in simulations and observations, with higher scatter at lower velocities. One might guess a physical cause of this trend is that star formation is a stochastic process, and thus when more stars are formed the variations average out. However, when compared to the halo velocity TF relations (see §3.2 below) we see the scatter is almost independent of mass, except for the very lowest mass haloes. Thus the variation in scatter is due to how the baryons influence $V_{\rm HI}$. The smaller scatter at high $V_{\rm HI}$ is due to the baryons contributing to $V_{\rm HI}$ (i.e., more baryons give higher velocity), while the larger scatter at small $V_{\rm HI}$ is due the variation in $V_{\rm HI}/V_{200}$, presumably due to $V_{\rm HI}$ tracing the rising part of the rotation curve, and thus being more sensitive to the exact radius the rotation is measured at.

Gas TF relation: The lower right panel shows the relation between neutral gas mass and HI circular velocity. The slopes of the simulations and observations are 3.61 ± 0.17 and 3.24 ± 0.28. The scatter is roughly independent of velocity at ~ 0.25 dex in both simulations and observations. Note that the SAM appears to over-predict the neutral gas mass. However, the SAM does not take into account the effects of ionization on the gas mass, which is substantial in the hydro simulations.

Baryonic TF relation: The upper panels show the baryonic TF relations. For the simulations the upper right panel shows the stars plus neutral gas within $0.2R_{200}$ (i.e., the observable baryons), while the upper left panel shows all the baryonic mass (i.e., stars plus gas) within R_{200}. The observations are only shown in the upper right panel and consist of stars plus neutral gas (atomic + molecular). The observed slope is 4.09±0.15 obtained by us using the same fitting technique we apply to the simulations. Reassuringly, this slope is consistent with fits from the original authors (McGaugh 2012; McGaugh & Schombert 2015). For the simulations the "observable" baryons have a slope of 3.97±0.09, in excellent agreement. It should be noted that the slope of the observed BTF strongly depends on the stellar mass-to-light ratio with values ranging from 3.4 to 4.0 for plausible M/L (Lelli et al. 2016). Here we adopt the calibrations of McGaugh (2012); McGaugh & Schombert (2015), which are on the high side of the plausible range and hence give steeper slopes. The full baryonic mass has slope of 3.11 ± 0.07, very close to the nominal ΛCDM value of 3. If one assumes $V_{\rm HI} \propto V_{200}$ thus implies a constant baryon mass fraction. However, as we see below, this assumption is not valid in our simulations. The actual baryon fractions are lower in lower mass haloes.

For galaxies with velocities in the range $50 \lesssim V_{\rm HI} \lesssim 250\,{\rm km\,s^{-1}}$ the observed scatter and intrinsic scatter in the BTF is $\simeq 0.18 - 0.23$ and $\simeq 0.11 \pm 0.03$ dex, respectively (Lelli et al. 2016). Over the full velocity range probed by the NIHAO simulations $20 \lesssim V_{\rm HI} \lesssim 240\,{\rm km\,s^{-1}}$ the total scatter about a power-law fit is 0.21 dex (Fig. 4). This is comparable to the observed scatter, but much larger than the estimated intrinsic scatter, nominally implying an inconsistency between our ΛCDM simulations and observations.

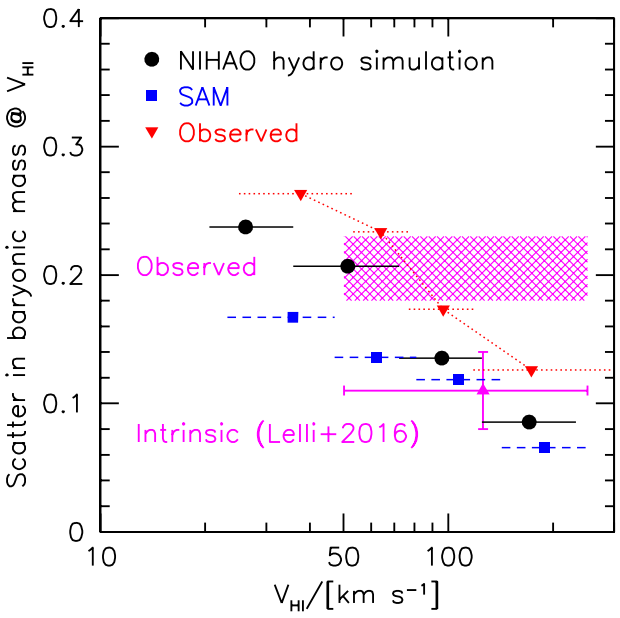

Figure 6. Scatter of the baryonic TF relation $M_{\rm gal}$ vs $V_{\rm HI}$ as a function of velocity. Black filled circles show results from the NIHAO simulations, while the blue squares dashed lines show results from the semi-analytic model used in Dutton (2012). Horizontal error bars correspond to the range in each velocity bin. Red triangles show the observed scatter using observations from McGaugh (2012) and McGaugh & Schombert (2015). The observed and intrinsic scatter from Lelli et al. (2016) are shown with the magenta shaded region and error bar, respectively.

However, in our simulations the scatter is strongly velocity dependent, with smaller scatter for higher velocity galaxies. Fig. 6 shows the scatter of the NIHAO simulations in quartile bins in velocity. Low velocity galaxies $20 \lesssim V_{\rm HI} \lesssim 70\,{\rm km\,s^{-1}}$ have scatter of $\simeq 0.20 - 0.24$ dex, while high velocity galaxies $70 \lesssim V_{\rm HI} \lesssim 240\,{\rm km\,s^{-1}}$ have scatter of 0.08 to 0.14 dex in good agreement with the observed intrinsic scatter on these scales. Fig. 6 also shows the semi-analytic model of Dutton (2012), which has a scatter that varies from 0.17 dex at low velocity to 0.07 dex at high velocity. The hydro simulations, which include more physical processes than the semi-analytic model, would nominally be expected to have larger scatter, which is indeed the case.

Given the tentative discrepancy we find between theory and observation at low velocities ($V_{\rm HI} \lesssim 70\,{\rm km\,s^{-1}}$) it will be interesting to study them further. Both to refine the predictions and obtain larger observational samples. An important consideration is that the rotation curves rise more slowly than in high mass galaxies (see Fig. 3). This means that the observed neutral hydrogen does not always reach the flat part of the rotation curve. It is debated whether of not this introduces a bias in the BTF at low masses (Brook et al. 2016; Lelli et al. 2016), and is thus an important topic for future studies to resolve.

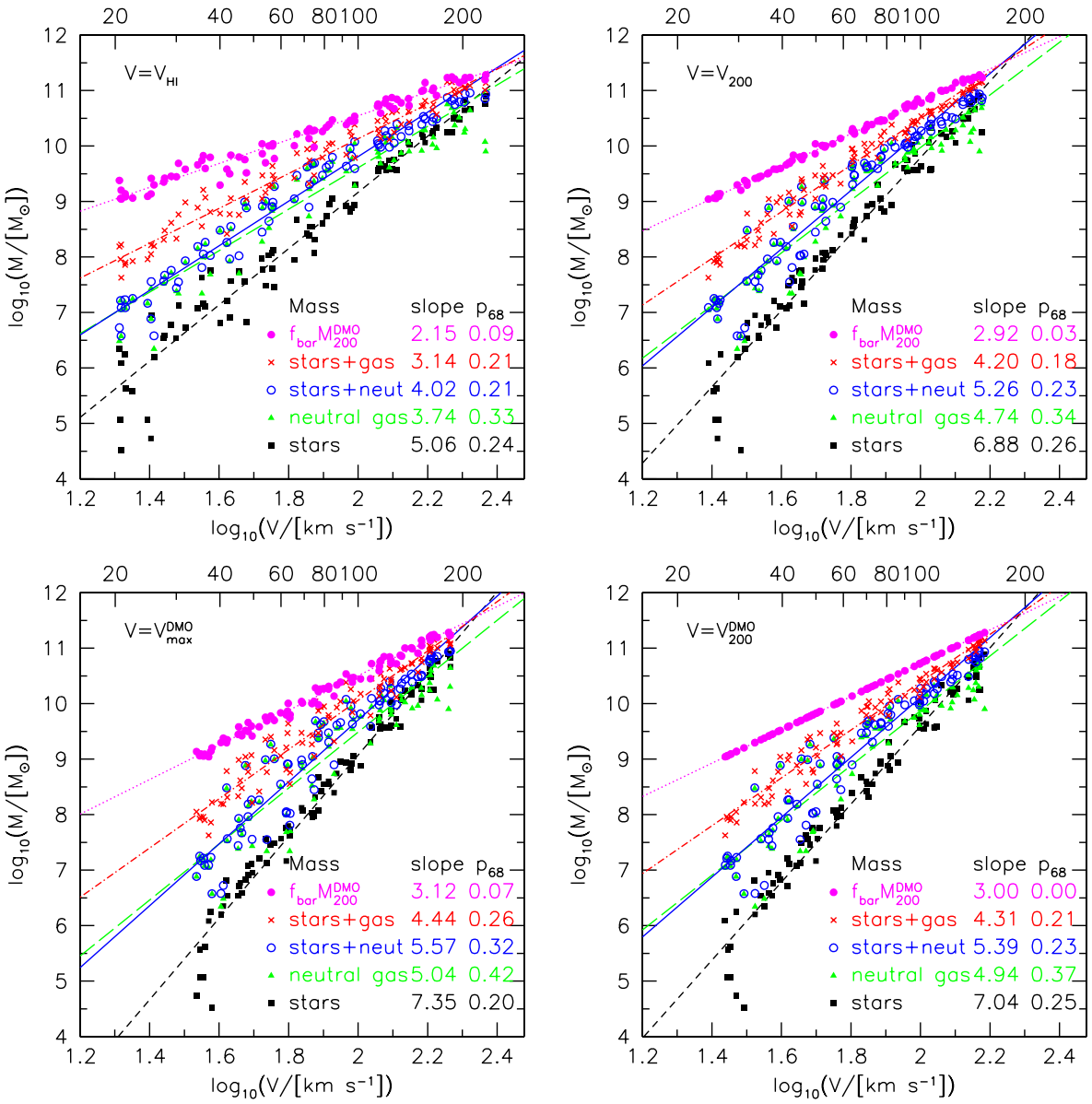

Figure 7. TF relations for a variety of masses and velocities. The masses are: stars (black squares), HI gas (green triangles), stars+ HI gas (blue open circles), stars + all gas (red crosses), and the total baryons associated with the dark matter only simulation, $(\Omega_{\rm b}/\Omega_{\rm m})M_{200}^{\rm DMO}$ (magenta filled circles). The velocities are: $V_{\rm HI}$ (upper left), V_{200} (upper right), $V_{\rm max}^{\rm DMO}$ (lower left), $V_{200}^{\rm DMO}$ (lower right). Each relation is fitted with a power-law, whose slope and scatter are given in the lower right corner. The data points for this figure are given in Table 1.

3.2 Dark halo velocity vs Mass relations

Fig. 7 shows the relations between various galaxy masses (total baryonic mass, galactic baryonic mass, stellar mass, and neutral gas mass) and various velocities ($V_{\rm HI}, V_{200}, V_{200}^{\rm DMO}, V_{\rm max}^{\rm DMO}$). Recall that V_{200} and $V_{200}^{\rm DMO}$ are by definition equivalent to halo mass since $V_{200} = (GM_{200}h)^{1/3}$. We fit each relation with a power-law over the full velocity range. The best fit relations are shown with lines the same color as the respective data points. The shallowest relation in each panel involves the total available baryonic mass (magenta), which by definition has a slope of 3 in the lower left panel. All of the relations with galaxy mass components have steeper slopes, corresponding to lower efficiency of galaxy formation (whether it be defined as cold gas, stars, or total baryons).

The upper right panel of Fig. 7 shows the relation between mass and virial velocity of the hydro simulation, V_{200}. All these relations are steeper than the corresponding relations using $V_{\rm HI}$. Note also that lower mass haloes have retained a smaller fraction of their baryons (compare red and magenta points and lines, see also Wang et al. 2016). The scatter increases as we go from the total baryonic mass (red crosses), to the galactic baryonic mass (blue circles), to the stellar mass (black squares), and finally to the neutral gas mass (green triangles). This supports the notion that the baryonic mass is a more fundamental galaxy property than either stellar or gas mass.

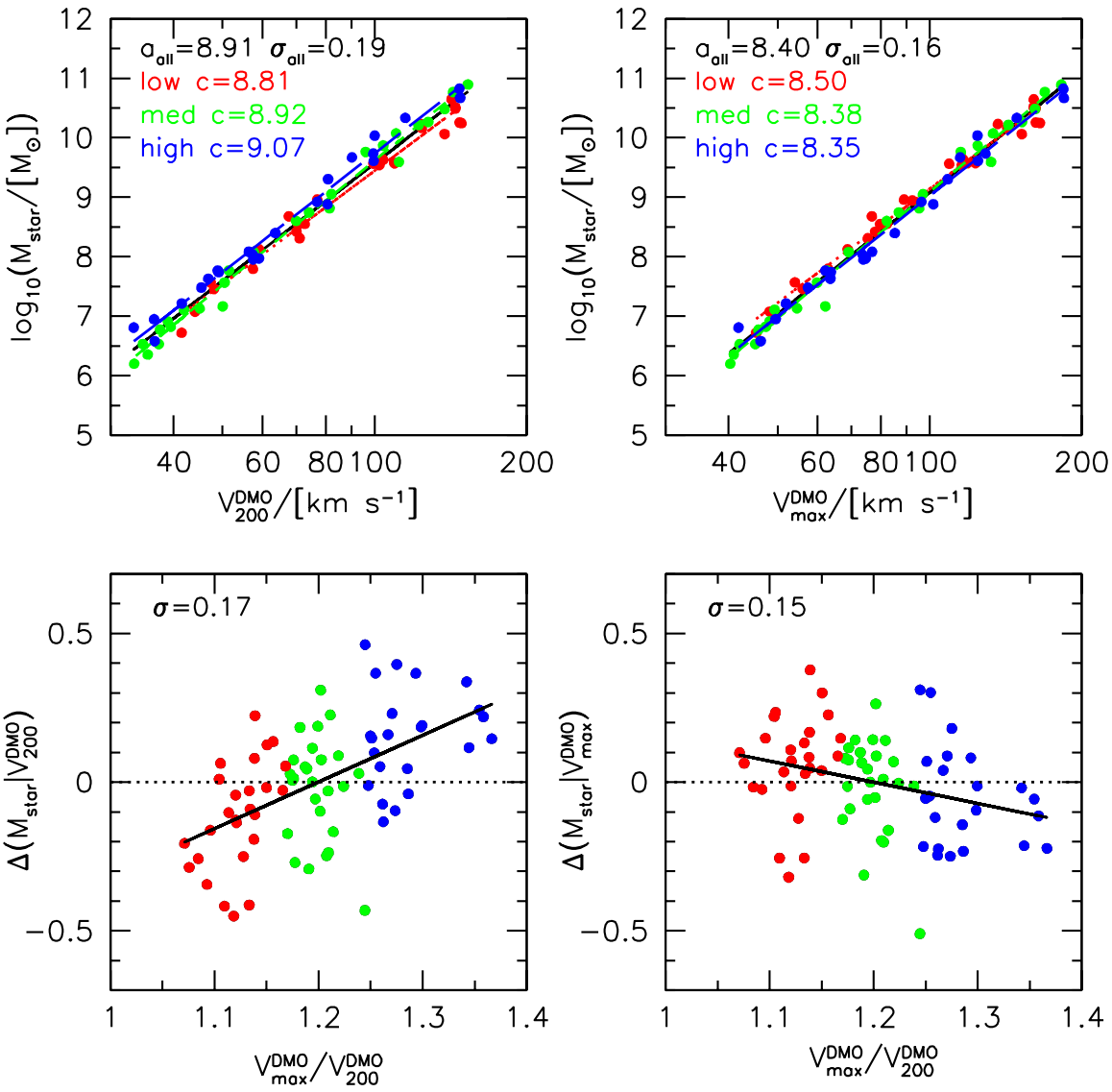

Figure 8. Dependence of scatter in stellar mass - halo velocity relation on halo concentration. The upper panels show the mass - velocity relations, using virial velocity, $V_{200}^{\rm DMO}$ (left), and maximum circular velocity, $V_{\rm max}^{\rm DMO}$ (right) from the DMO simulations. The zero point, $a_{\rm all}$, and scatter, $\sigma_{\rm all}$ from a linear fit (solid black lines) are shown at the top of each panel. The subsequent numbers show the zero points for fits to low, average, and high concentration haloes. The lower panels show the residuals about the best fit relation vs $V_{\rm max}^{\rm DMO}/V_{200}^{\rm DMO}$ which is our proxy for halo concentration. In all panels points are color coded by concentration, with red for low, green for average, and blue for high. At fixed virial velocity higher concentration haloes are offset to higher stellar masses, while at fixed maximum circular velocity higher concentration haloes are offset to lower stellar masses. The scatter about the mass residual vs concentration relation is given in the upper left corner, and shows that including concentration reduces the scatter in the mass - velocity relation.

The lower left panel shows results using the maximum circular velocity from the DMO simulation, $V_{\rm max}^{\rm DMO}$, while the lower right panel uses the virial circular velocity from the DMO simulation, $V_{200}^{\rm DMO}$. The slopes are slightly steeper with $V_{200}^{\rm DMO}$ than V_{200} due to increased mass loss from lower mass haloes, and steeper still using $V_{\rm max}^{\rm DMO}$ because lower mass haloes have higher $V_{\rm max}^{\rm DMO}/V_{200}$ due to the higher average concentrations (recall the concentration vs velocity relation for CDM haloes goes like $c \propto M_{200}^{-0.1} \propto V_{200}^{-0.3}$).

Comparing the different panels in Fig. 7 we see that stellar mass correlates better with maximum halo velocity than virial velocity, while cold gas mass, and total baryonic mass correlates better with virial velocity than maximum velocity. Thus there is no single velocity definition that minimizes the scatter in all baryonic components.

4 IMPLICATIONS FOR HALO ABUNDANCE MATCHING

The halo abundance matching technique is a powerful way to link the masses of galaxies to the masses of dark matter

haloes, under the assumption of ΛCDM and cosmological parameters (Conroy & Wechsler 2009). It can be used to understand how stars form over cosmic time. In its simplest form, the ansatz is that more massive galaxies live in more massive dark matter haloes. In our simulations scatter in stellar mass at fixed halo virial or maximum circular velocity is small $\simeq 0.20$ dex, and independent of halo velocity for $30 \lesssim V_{200} \lesssim 160\,\mathrm{km\,s^{-1}}$. This supports the halo abundance matching approach for central haloes. At the lowest halo masses we probe $V_{200} \sim 25\,\mathrm{km\,s^{-1}}$ the scatter starts to increase, consistent with other simulation studies (e.g., Sawala et al. 2016).

Using observations of the projected two-point galaxy clustering Reddick et al. (2013) showed that the peak circular velocity of the dark matter halo (over the history of a halo) is more closely related to stellar mass than the virial velocity of the halo. Maximum circular velocity (either at a given time, or over the history of a halo) is often preferred over halo mass (or virial velocity) because (1) $V_{\rm max}^{\rm DMO}$ does not depend on the (somewhat arbitrary) definition of halo mass, (2) $V_{\rm max}^{\rm DMO}$ is less sensitive to the mass stripping that sub-haloes experience, (3) $V_{\rm max}^{\rm DMO}$ probes a smaller scale which presumably has more to do with galaxy formation than the virial scale.

In our galaxy formation simulations we indeed find that the maximum circular velocity (at the present day) of the dark matter only simulation yields a smaller global scatter (0.20 dex) in stellar mass than the virial velocity (0.25 dex) of the hydro or DMO simulation (Fig. 7). Removing the haloes with $V_{200}^{\rm DMO} < 32\,\mathrm{km\,s^{-1}}$, which have very large scatter in stellar mass, results in smaller scatters of 0.17 dex and 0.19 dex for $V_{\rm max}^{\rm DMO}$ and V_{200}, respectively.

Going, further, there has been recent discussion in the literature of a dependence of the abundance matching on the concentration of the dark matter halo (Lehmann et al. 2015; Mao et al. 2015; Paranjape et al. 2015). We thus investigate further whether an additional parameter, or a different definition of halo velocity yields a tighter stellar mass - halo velocity relation.

The left panels of Fig. 8 show the stellar mass vs halo virial velocity relation and its dependence on halo concentration. Here as a proxy for concentration we use the ratio between maximum and virial circular velocities of the DMO simulation: $V_{\rm max}^{\rm DMO}/V_{200}^{\rm DMO}$. At fixed halo velocity, $V_{200}^{\rm DMO}$, there is a trend with concentration such that higher concentration haloes have higher stellar masses. This is plausibly because higher concentration haloes, on average, form earlier (e.g., Wechsler et al. 2002), and thus have more time to form stars. The overall scatter is 0.19 dex (upper left), and can be reduced to 0.17 dex (lower left) by including the correlation with concentration.

The right panels of Fig. 8 show the same results by using the maximum circular velocity of the halo in place of the virial velocity. Now the correlation with concentration is weaker, and of the opposite sign. The change in sign of the correlation suggests that a velocity measured somewhere between the virial radius and $0.2R_{200}$ (where $V_{\rm max}^{\rm DMO}$ occurs) would produce a tighter correlation with galaxy stellar mass. The overall scatter is 0.17 dex (upper right), and can be reduced to 0.14 dex (lower right) by including the correlation with concentration.

Fig. 9 shows the scatter in the $M_{\rm star} - V$ relation with

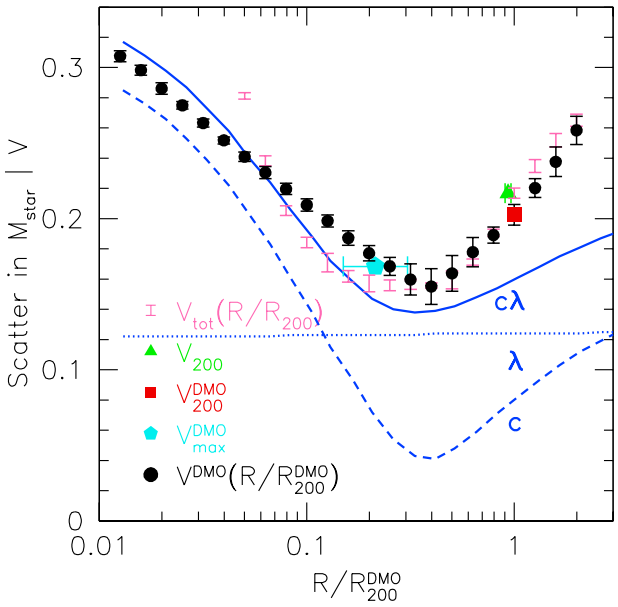

Figure 9. Scatter of the stellar mass vs halo velocity relation for different halo velocities. Black circles show velocity measured at various fractions of the virial radius in the DMO simulations. Error bars are from Jackknife re-sampling. Pink error bars show results using the total circular velocity at various radii in the hydro simulations. The scatter is minimized for $R/R_{200}^{\rm DMO} \simeq 0.4$, providing a tighter relation than when using the maximum circular velocity of the DMO simulation (cyan pentagon) or virial velocity of the DMO (red square) or hydro (green triangle) simulation. The solid blue lines show results from the SAM which includes scatter in concentration and spin ($c\lambda$). The SAM also has a minimum scatter at $R/R_{200}^{\rm DMO} \simeq 0.4$. Models run with just scatter in c (dashed line), or λ (dotted line) shows that concentration drives this minimum.

velocity measured at various fractions of the virial radius, R/R_{200} in the DMO simulations. We find that the minimum scatter of 0.15 dex occurs when the circular velocity is measured at $\sim 0.4R_{200}$. This corresponds to an over-density of $\sim 1000\rho_{\rm crit}$. This scatter is even smaller than when using the maximum circular velocity of the DMO simulation (0.17 dex), which typically occurs at $0.2R_{200}$ (blue pentagon). For reference the maximum circular velocity occurs at $R_{V_{\rm max}} \simeq 2.2R_{200}/c$.

Observationally, Lehmann et al. (2015), show that low redshift clustering measurements from SDSS prefer a moderate amount of concentration dependence (more than would be indicated by matching galaxy luminosity to the peak halo mass, and less than would be indicated by matching to the peak halo circular velocity). Defining the halo velocity as

$$V_\alpha = V_{200}(V_{\rm max}/V_{200})^\alpha \qquad (2)$$

Lehmann et al. (2015) found the scatter in stellar mass was minimized at $\sigma = 0.17^{+0.03}_{-0.05}$ for $\alpha = 0.57^{+0.20}_{-0.27}$. We find similar results with our hydrodynamical simulations. Fig. 10 shows the scatter in the stellar mass vs $V_\alpha^{\rm DMO}$ relation as a function of α. The scatter is minimized at $\alpha \simeq 0.7$.

To help understand the origin of the results in Fig. 8-10 we show results from the SAM of Dutton (2012). Recall that there are just two parameters that can cause variation

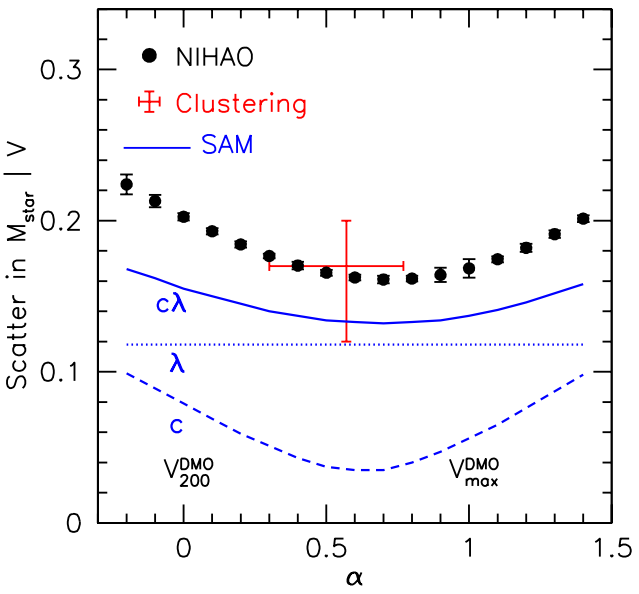

Figure 10. Scatter of the stellar mass vs halo velocity relation for $V_\alpha^{\rm DMO} = V_{200}(V_{\rm max}/V_{200})^\alpha$. The scatter is minimized for $\alpha \simeq 0.7$, for both the NIHAO hydro simulations (black points) and the SAM (solid blue line), consistent with results from clustering (Lehmann et al. 2015, red error bar). The dashed line shows a SAM that includes only scatter in halo concentration, while the dotted line shows a model that only includes scatter in halo spin.

in galaxy properties: halo concentration, c, and halo spin, λ. Remarkably, the SAM has a minimum scatter at the same radii $R \sim 0.4R_{200}$ and $\alpha \sim 0.7$. The fact we find similar results for the SAM as the full hydro simulation suggests there is a simple physical origin of these trends. In addition to the default model, we run models with only scatter in c or λ. These show that the minimum in scatter is driven solely by the scatter in concentration parameter. Since the concentration parameter is strongly correlated with the mass accretion history, we suggest that the formation history of the halo is the underlying physical origin of these trends. The exact reason why this results in a preferable scale of $0.4R_{200}$ remains to be determined.

5 SUMMARY

We study the scaling relations between galaxy mass and circular velocity in halos of mass $10^{10} \lesssim M_{200} \lesssim 10^{12}{\rm M}_\odot$. We use a sample of 83 fully cosmological galaxy formation simulations from the NIHAO project (Wang et al. 2015), and the semi-analytic model of Dutton (2012). We summarize our results as follows:

- The simulations are consistent with the observed stellar, cold gas, and baryonic Tully-Fisher relations (Fig. 4).
- For the baryonic Tully-Fisher relation, our simulations have a small scatter of 0.08-0.14 dex in mass for $70 \lesssim V_{\rm HI} \lesssim 240\,{\rm km\,s^{-1}}$, consistent with observational estimates (Fig. 6). At lower velocities $20 \lesssim V_{\rm HI} \lesssim 70\,{\rm km\,s^{-1}}$ our simulations predict larger scatters of 0.2 to 0.25 dex, potentially in conflict with observations.
- The scatter in stellar mass at fixed halo velocity is constant for $30 < V < 160\,{\rm km\,s^{-1}}$. The maximum circular velocity of the DMO simulation, $V_{\rm max}^{\rm DMO}$ provides a better predictor of the stellar mass, than the virial velocity of the DMO (or hydro) simulation (Fig. 7). However, for gas and baryonic mass, virial velocity is a better predictor than maximum velocity.
- The normalization of the stellar mass vs virial velocity relation is correlated with halo concentration. These correlations are substantially reduced in the stellar mass vs $V_{\rm max}^{\rm DMO}$ relation (Fig. 8).
- Measuring the circular velocity at $\simeq 0.4R_{200}^{\rm DMO}$ minimizes the scatter in stellar mass vs halo velocity relation at 0.15 dex (Fig. 9).
- Defining the halo circular velocity as $V_\alpha = V_{200}^{\rm dmo}(V_{\rm max}^{\rm DMO}/V_{200}^{\rm DMO})^\alpha$, where $\alpha = 0$ corresponds to virial velocity and $\alpha = 1$ corresponds to maximum circular velocity, we find the scatter is minimized at 0.16 dex for $\alpha = 0.7$ (Fig. 10), consistent with clustering based constraints (Lehmann et al. 2015).

The small scatter in the Tully-Fisher relations from the NIHAO simulations and the semi-analytic model of Dutton (2012) point to the simplicity of galaxy formation due to the self-regulation between star formation and energy feedback from massive stars.

The dependence of scatter in the stellar mass vs halo velocity with concentration appears to be a fundamental property of galaxy formation in a ΛCDM universe, and thus can be used to improve the accuracy of halo abundance matching models.

ACKNOWLEDGMENTS

This research was carried out on the High Performance Computing resources at New York University Abu Dhabi; on the THEO cluster of the Max-Planck-Institut für Astronomie and the HYDRA cluster at the Rechenzentrum in Garching; and the Milky Way supercomputer, which is funded by the Deutsche Forschungsgemeinschaft (DFG) through Collaborative Research Center (SFB 881) "The Milky Way System" (subproject Z2) and hosted and co-funded by the Jülich Supercomputing Center (JSC). We greatly appreciate the contributions of all these computing allocations. TB and TAG were supported by the Sonderforschungsbereich SFB 881 "The Milky Way System" (subprojects A1 and A2) of the German Research Foundation (DFG). The analysis made use of the pynbody package (Pontzen et al. 2013). XK acknowledge the support from NSFC project No.11333008 and the "Strategic Priority Research Program the Emergence of Cosmological Structures" of the CAS(No.XD09010000).

REFERENCES

Behroozi, P. S., Wechsler, R. H., & Conroy, C. 2013, ApJ, 770, 57
Bell, E. F., & de Jong, R. S. 2001, ApJ, 550, 212
Blumenthal, G. R., Faber, S. M., Flores, R., & Primack, J. R., 1986, ApJ, 301, 27
Bradford, J. D., Geha, M. C., & van den Bosch, F. C. 2016, arXiv:1602.02757

Brook, C. B., Santos-Santos, I., & Stinson, G. 2016, MNRAS, 459, 638
Chan, T. K., Kereš, D., Oñorbe, J., et al. 2015, MNRAS, 454, 2981
Conroy, C., & Wechsler, R. H. 2009, ApJ, 696, 620
Courteau, S., Dutton, A. A., van den Bosch, F. C., MacArthur, L. A., Dekel, A., McIntosh, D. H., & Dale, D. A. 2007, ApJ, 671, 203
Desmond, H., & Wechsler, R. H. 2015, MNRAS, 454, 322
Dutton, A. A., van den Bosch, F. C., Dekel, A., & Courteau, S. 2007, ApJ, 654, 27
Dutton, A. A., & van den Bosch, F. C. 2009, MNRAS, 396, 141
Dutton, A. A., Conroy, C., van den Bosch, F. C., Prada, F., & More, S. 2010, MNRAS, 407, 2
Dutton, A. A., Conroy, C., van den Bosch, F. C., et al. 2011, MNRAS, 416, 322
Dutton, A. A. 2012, MNRAS, 424, 3123
Dutton, A. A., & Macciò, A. V. 2014, MNRAS, 441, 3359
Dutton, A. A., Macciò, A. V., Frings, J., et al. 2016a, MNRAS, 457, L74
Faber, S. M., & Jackson, R. E. 1976, ApJ, 204, 668
Gill, S. P. D., Knebe, A., & Gibson, B. K. 2004, MNRAS, 351, 399
Gnedin, O. Y., Kravtsov, A. V., Klypin, A. A., & Nagai, D. 2004, ApJ, 616, 16
Governato, F., Willman, B., Mayer, L., et al. 2007, MNRAS, 374, 1479
Gutcke, T. A., Stinson, G. S., Macciò, A. V., Wang, L., & Dutton, A. A. 2016, arXiv:1602.06956v2, MNRAS in press
Hudson, M. J., Gillis, B. R., Coupon, J., et al. 2015, MNRAS, 447, 298
Knollmann, S. R., & Knebe, A. 2009, ApJS, 182, 608
Keller, B. W., Wadsley, J., Benincasa, S. M., & Couchman, H. M. P. 2014, MNRAS, 442, 3013
Kravtsov, A. V. 2013, ApJL, 764, L31
Leauthaud, A., Tinker, J., Bundy, K., et al. 2012, ApJ, 744, 159
Lehmann, B. V., Mao, Y.-Y., Becker, M. R., Skillman, S. W., & Wechsler, R. H. 2015, arXiv:1510.05651
Lelli, F., McGaugh, S. S., & Schombert, J. M. 2016, ApJL, 816, L14
Macciò, A. V., Udrescu, S. M., Dutton, A. A., et al. 2016, MNRAS, 463, L69
Mandelbaum, R., Seljak, U., Kauffmann, G., Hirata, C. M., & Brinkmann, J. 2006, MNRAS, 368, 715
Mao, Y.-Y., Williamson, M., & Wechsler, R. H. 2015, ApJ, 810, 21
Marinacci, F., Pakmor, R., & Springel, V. 2014, MNRAS, 437, 1750
McGaugh, S. S., Schombert, J. M., Bothun, G. D., & de Blok, W. J. G. 2000, ApJL, 533, L99
McGaugh, S. S. 2012, AJ, 143, 40
McGaugh, S. S., & Schombert, J. M. 2015, ApJ, 802, 18
Mo, H. J., Mao, S., & White, S. D. M. 1998, MNRAS, 295, 319
More, S., van den Bosch, F. C., Cacciato, M., et al. 2011, MNRAS, 410, 210
Moster, B. P., Somerville, R. S., Maulbetsch, C., et al. 2010, ApJ, 710, 903
Navarro, J. F., & Steinmetz, M. 2000, ApJ, 538, 477
Papastergis, E., Giovanelli, R., Haynes, M. P., & Shankar, F. 2015, A&A, 574, A113
Paranjape, A., Kovač, K., Hartley, W. G., & Pahwa, I. 2015, MNRAS, 454, 3030
Planck Collaboration, Ade, P. A. R., Aghanim, N., et al. 2014, A&A, 571, A16
Pontzen, A., Roškar, R., Stinson, G., & Woods, R. 2013, Astrophysics Source Code Library, 1305.002
Rahmati, A., Schaye, J., Pawlik, A. H., & Raičevič, M. 2013, MNRAS, 431, 2261
Reddick, R. M., Wechsler, R. H., Tinker, J. L., & Behroozi, P. S. 2013, ApJ, 771, 30
Reyes, R., Mandelbaum, R., Gunn, J. E., Pizagno, J., & Lackner, C. N. 2011, MNRAS, 417, 2347
Sawala, T., Frenk, C. S., Fattahi, A., et al. 2016, MNRAS, 457, 1931
Stinson, G., Seth, A., Katz, N., et al. 2006, MNRAS, 373, 1074
Stinson, G. S., Brook, C., Macciò, A. V., et al. 2013, MNRAS, 428, 129
Tollet, E., Macciò, A. V., Dutton, A. A., et al. 2016, MNRAS, 456, 3542
Tully, R. B., & Fisher, J. R. 1977, A&A, 54, 661
Wadsley, J. W., Stadel, J., & Quinn, T. 2004, NewA, 9, 137
Wang, L., Dutton, A. A., Stinson, G. S., Macciò, A. V., Penzo, C., Kang, X., Keller, B. W., Wadsley, J. 2015, MNRAS, 454, 83
Wang, L., Dutton, A. A., Stinson, G. S., et al. 2016, arXiv:1601.00967
Wechsler, R. H., Bullock, J. S., Primack, J. R., Kravtsov, A. V., & Dekel, A. 2002, ApJ, 568, 52
Yang, X., Mo, H. J., & van den Bosch, F. C. 2003, MNRAS, 339, 1057

Table 1. Data from NIHAO simulations from Fig. 7. All logarithms are base 10. Sizes are in units of kpc, velocities in $\mathrm{km\,s^{-1}}$, and masses in $\mathrm{M_\odot}$. Column (1) NIHAO simulation ID, column (2) HI radius, column (3) circular velocity measured at the HI radius, column (4) maximum circular velocity of the dark matter only simulation, column (5) virial circular velocity from the hydro simulation, column (6) virial circular velocity from the dark matter only simulation, column (7) stellar mass, column (8) neutral gas mass, column (9) galaxy baryonic mass (column 7 plus column 8), column (10) baryonic mass inside the virial radius of the hydro simulation, column (11) baryonic mass associated with the dark matter only simulation, $M_{\rm bar}^{\rm DMO} \equiv (\Omega_{\rm b}/\Omega_{\rm m}) M_{200}^{\rm DMO}$.

ID	$\log(R_{\rm HI})$ [kpc]	$\log(V_{\rm HI})$ [$\mathrm{km\,s^{-1}}$]	$\log(V_{\rm max}^{\rm DMO})$ [$\mathrm{km\,s^{-1}}$]	$\log(V_{200})$ [$\mathrm{km\,s^{-1}}$]	$\log(V_{200}^{\rm DMO})$ [$\mathrm{km\,s^{-1}}$]	$\log(M_{\rm star})$ [$\mathrm{M_\odot}$]	$\log(M_{\rm neut})$ [$\mathrm{M_\odot}$]	$\log(M_{\rm gal})$ [$\mathrm{M_\odot}$]	$\log(M_{\rm bar})$ [$\mathrm{M_\odot}$]	$\log(M_{\rm bar}^{\rm DMO})$
(1)	(2)	(3)	(4)	(5)	(6)	(7)	(8)	(9)	(10)	(11)
g4.36e09	-0.032	1.318	1.579	1.483	1.492	4.518	6.574	6.578	8.222	9.205
g4.99e09	-0.086	1.351	1.544	1.406	1.445	5.575	7.244	7.253	7.926	9.064
g5.22e09	-0.036	1.394	1.547	1.420	1.455	5.070	7.164	7.167	7.961	9.094
g5.41e09	-0.244	1.319	1.570	1.390	1.438	6.084	7.044	7.089	7.627	9.043
g5.59e09	-0.208	1.329	1.576	1.424	1.471	6.240	7.184	7.231	7.860	9.142
g5.84e09	-0.108	1.316	1.555	1.412	1.443	5.064	7.214	7.217	7.961	9.056
g7.05e09	-0.004	1.313	1.612	1.494	1.551	6.355	6.484	6.725	8.191	9.381
g7.34e09	-0.187	1.330	1.558	1.414	1.454	5.626	7.074	7.089	7.900	9.089
g9.26e09	0.097	1.404	1.535	1.416	1.470	4.730	6.884	6.887	8.052	9.138
g1.09e10	0.787	1.603	1.622	1.501	1.523	6.810	8.474	8.483	8.786	9.298
g1.18e10	0.068	1.441	1.624	1.500	1.541	6.531	7.524	7.566	8.312	9.352
g1.23e10	0.170	1.413	1.605	1.473	1.524	6.201	6.344	6.580	8.197	9.300
g1.44e10	0.610	1.679	1.676	1.563	1.596	6.826	8.884	8.888	9.042	9.517
g1.50e10	0.107	1.477	1.655	1.536	1.573	6.531	7.384	7.441	8.332	9.446
g1.57e10	-0.056	1.405	1.695	1.524	1.563	6.950	7.434	7.557	8.216	9.418
g1.88e10	0.562	1.622	1.715	1.578	1.618	7.215	8.224	8.264	8.418	9.583
g1.89e10	0.427	1.560	1.693	1.597	1.623	7.108	8.234	8.265	9.073	9.596
g1.90e10	0.500	1.538	1.684	1.614	1.645	7.077	8.154	8.189	8.891	9.662
g1.92e10	0.297	1.503	1.656	1.586	1.618	6.721	7.904	7.931	8.987	9.582
g1.95e10	0.049	1.443	1.665	1.533	1.565	6.581	7.634	7.671	8.477	9.422
g2.09e10	0.986	1.630	1.683	1.560	1.590	6.914	7.924	7.964	8.772	9.500
g2.34e10	0.367	1.483	1.737	1.623	1.654	7.133	7.344	7.552	8.767	9.690
g2.39e10	0.193	1.462	1.661	1.541	1.575	6.772	7.714	7.761	8.618	9.454
g2.63e10	0.158	1.551	1.803	1.630	1.671	7.631	7.344	7.812	8.555	9.741
g2.64e10	0.990	1.759	1.749	1.658	1.682	7.459	9.264	9.271	9.402	9.775
g2.80e10	0.549	1.634	1.777	1.634	1.703	7.565	8.504	8.551	9.058	9.837
g2.83e10	0.835	1.733	1.759	1.621	1.657	7.481	8.994	9.007	9.161	9.699
g2.94e10	0.348	1.574	1.793	1.656	1.689	7.764	7.684	8.027	8.812	9.797
g3.19e10	0.352	1.554	1.793	1.665	1.699	7.167	7.994	8.054	9.212	9.826
g3.44e10	1.128	1.754	1.799	1.719	1.759	7.797	8.874	8.909	9.644	10.005
g3.67e10	0.484	1.657	1.805	1.653	1.692	7.739	7.704	8.023	8.759	9.803
g3.93e10	0.852	1.674	1.733	1.659	1.675	7.567	8.974	8.991	9.355	9.755
g4.27e10	0.925	1.724	1.797	1.697	1.711	7.767	8.884	8.916	9.471	9.863
g4.48e10	0.849	1.755	1.837	1.748	1.771	8.122	8.924	8.988	9.476	10.042
g4.86e10	0.922	1.873	1.886	1.725	1.751	8.082	9.364	9.386	9.471	9.981
g4.94e10	0.648	1.743	1.867	1.728	1.759	8.033	8.524	8.645	9.268	10.005
g4.99e10	0.818	1.752	1.840	1.717	1.761	8.078	8.834	8.904	9.296	10.011
g5.05e10	0.580	1.724	1.874	1.698	1.771	7.971	8.274	8.449	9.051	10.041
g6.12e10	1.036	1.816	1.869	1.719	1.760	7.954	9.014	9.050	9.424	10.007
g6.37e10	1.236	1.875	1.877	1.839	1.852	8.310	9.674	9.692	10.043	10.283
g6.77e10	0.958	1.824	1.885	1.810	1.830	8.679	9.394	9.470	9.872	10.219
g6.91e10	0.876	1.858	1.931	1.770	1.803	8.396	8.734	8.898	9.322	10.138
g6.96e10	1.120	1.860	1.915	1.805	1.861	8.552	9.224	9.308	9.741	10.313
g8.89e10	0.931	1.897	1.915	1.809	1.845	8.601	9.414	9.476	9.794	10.262
g9.59e10	1.122	1.853	1.892	1.803	1.845	8.419	9.594	9.622	9.944	10.264
g1.05e11	1.083	1.908	1.939	1.844	1.870	8.744	9.554	9.616	9.932	10.338
g1.08e11	1.108	1.966	1.984	1.847	1.886	8.922	9.544	9.637	9.845	10.387
g1.37e11	0.876	1.990	2.036	1.877	1.908	9.303	9.284	9.594	9.787	10.452
g1.52e11	1.205	1.982	2.007	1.886	1.906	8.882	9.764	9.817	10.179	10.448
g1.57e11	1.040	1.926	1.986	1.886	1.914	9.053	9.714	9.800	10.050	10.471
g1.59e11	1.338	1.977	1.979	1.896	1.911	8.813	9.924	9.956	10.263	10.461
g1.64e11	1.184	1.990	1.965	1.917	1.936	8.944	10.044	10.077	10.385	10.536

Table 1. – continued.

ID (1)	$\log(R_{\rm HI})$ (2)	$\log(V_{\rm HI})$ (3)	$\log(V_{\rm max}^{\rm DMO})$ (4)	$\log(V_{200})$ (5)	$\log(V_{200}^{\rm DMO})$ (6)	$\log(M_{\rm star})$ (7)	$\log(M_{\rm neut})$ (8)	$\log(M_{\rm gal})$ (9)	$\log(M_{\rm bar})$ (10)	$\log(M_{\rm bar}^{\rm DMO})$ (11)
g2.04e11	0.915	2.065	2.060	1.927	1.955	9.670	9.684	9.978	10.139	10.593
g2.19e11	0.980	1.917	1.949	1.860	1.886	8.961	9.564	9.661	10.039	10.387
g2.39e11	0.876	2.103	2.062	1.958	1.982	9.762	9.744	10.054	10.248	10.675
g2.41e11	0.981	2.060	2.095	1.955	1.998	9.610	9.804	10.019	10.232	10.723
g2.42e11	0.907	2.090	2.110	1.963	1.997	9.736	9.614	9.980	10.120	10.720
g2.54e11	0.931	2.057	2.063	1.963	2.009	9.540	9.884	10.046	10.305	10.756
g2.57e11	1.157	2.147	2.095	1.976	2.000	10.033	9.904	10.274	10.433	10.729
g3.06e11	0.930	2.124	2.095	1.985	2.017	9.868	9.874	10.172	10.392	10.779
g3.21e11	1.080	2.056	2.039	1.981	1.998	9.563	9.944	10.095	10.453	10.721
g3.23e11	1.141	1.869	1.902	1.804	1.848	8.544	9.644	9.677	9.953	10.272
g3.49e11	1.206	2.097	2.121	2.030	2.048	9.592	10.164	10.267	10.607	10.872
g3.55e11	1.318	2.112	2.091	2.029	2.039	9.575	10.324	10.395	10.635	10.846
g3.59e11	1.143	2.077	2.066	2.002	2.017	9.635	10.164	10.276	10.539	10.778
g3.61e11	1.172	2.226	2.172	2.032	2.061	10.333	9.964	10.487	10.567	10.910
g3.71e11	1.426	2.145	2.125	2.024	2.042	10.073	10.064	10.369	10.626	10.855
g5.02e11	1.356	2.188	2.153	2.074	2.093	10.162	10.294	10.534	10.731	11.008
g5.31e11	1.387	2.183	2.156	2.062	2.087	10.214	9.914	10.391	10.716	10.989
g5.36e11	1.116	2.193	2.182	2.101	2.138	10.063	10.284	10.488	10.816	11.143
g5.38e11	1.203	2.217	2.183	2.091	2.106	10.265	10.154	10.514	10.749	11.046
g5.46e11	1.161	2.080	2.075	1.991	2.040	9.572	10.064	10.185	10.446	10.848
g5.55e11	1.003	2.214	2.135	2.059	2.091	10.232	10.024	10.441	10.650	11.002
g6.96e11	1.137	2.278	2.206	2.122	2.159	10.513	10.374	10.750	10.936	11.207
g7.08e11	1.259	2.291	2.208	2.123	2.138	10.482	10.514	10.799	10.972	11.143
g7.44e11	1.212	2.257	2.210	2.178	2.168	10.253	10.754	10.873	11.157	11.232
g7.55e11	1.342	2.276	2.209	2.138	2.160	10.490	10.604	10.852	11.017	11.208
g7.66e11	1.036	2.365	2.228	2.143	2.155	10.771	10.074	10.850	11.006	11.194
g8.06e11	1.124	2.306	2.206	2.146	2.152	10.647	10.244	10.791	11.043	11.185
g8.13e11	1.568	2.308	2.265	2.152	2.168	10.824	10.304	10.939	11.060	11.231
g8.26e11	1.437	2.322	2.265	2.157	2.169	10.669	10.644	10.957	11.088	11.236
g8.28e11	1.288	2.270	2.218	2.176	2.172	10.245	10.684	10.819	11.152	11.244
g1.12e12	1.237	2.367	2.260	2.170	2.185	10.894	9.904	10.937	11.138	11.282